Selective laser sintering of an amorphous polymer—simulations and experiments

T H C Childs*, M Berzins, G R Ryder and **A Tontowi**
Departments of Mechanical Engineering and Computer Studies, The University of Leeds, UK

Abstract: Thermal and powder densification modelling of the selective laser sintering of amorphous polycarbonate is reported. Three strategies have been investigated: analytical, adaptive mesh finite difference and fixed mesh finite element. A comparison between the three and experimental results is used to evaluate their ability reliably to predict the behaviour of the physical process. The finite difference and finite element approaches are the only ones that automatically deal with the non-linearities of the physical process that arise from the variation in the thermal properties of the polymer with density during sintering, but the analytical model has some value, provided appropriate mean values are used for thermal properties. Analysis shows that the densification and linear accuracies due to sintering are most sensitive to changes in the activation energy and heat capacity of the polymer, with a second level of sensitivities that includes powder bed density and powder layer thickness. Simulations of the manufacture of hollow cylinders and T-pieces show feature distortions due to excessive depth of sintering at downward facing surfaces in the powder bed. In addition to supporting the modelling, the experiments draw attention to the importance of sintering machine hardware and software controls.

Keywords: rapid prototyping, selective laser sintering, polycarbonate

NOTATION

A	Arrhenius coefficient (s^{-1})
C	specific heat (J/kg)
d	laser beam diameter (mm)
dh_i	thickness of powder layer i after sintering (variable) (mm)
E	Young's modulus (GPa)
E/R	ratio of sintering activation energy to the gas constant (K^{-1})
k	conductivity (variable) (W/m K)
k_{solid}	conductivity of solid material (W/m K)
m_s, m_t	space and time monitors in adaptive finite difference calculation
P	laser power (W)
q	laser heat flux (W/mm^2)
s	laser scan spacing (mm)
t_{layer}	powder layer thickness (set value) (mm)
T	temperature (°C or K)
T_s, T_t	space and time tolerance factors in adaptive mesh finite difference calculation
U	laser scan speed (mm/s)
V	equivalent laser scan speed $= (U/w)s$ (mm/s)
w	laser scan vector length (or part width) (mm)
x, y, z, t	basic position and time variables (mm and s)
α	heat absorption coefficient
α_s, α_t	weighting factors in adaptive finite difference calculation
δx, δy, δz	part oversize in x, y and z directions (mm)
Δh_i	thickness of powder layer i before sintering (variable) (mm)
Δy, Δz	initial mesh spacing, adaptive finite difference calculation (mm)
ε	porosity
θ, θ_s	weighting factors in the finite element calculations
κ	thermal diffusivity (mm^2/s)
ρ	density (variable) (kg/m^3)

The MS was received on 20 July 1998 and was accepted after revision for publication on 11 November 1998.
**Corresponding author: Department of Mechanical Engineering, The University of Leeds, Leeds LS2 9JT, UK.*

ρ_{max}	maximum attainable density in sintering (kg/m^3)
ρ_{powder}	density of powder bed (kg/m^3)
ρ_{solid}	density of solid (kg/m^3)
σ_f	tensile failure stress in bending (MPa)
σ_y	tensile yield stress in bending (MPa)

1 INTRODUCTION

This paper reports thermal modelling of the selective laser sintering process, undertaken to gain understanding of observed limits of accuracy. A tool has been developed, able to predict, in two dimensions and for amorphous materials, the influence of laser scanning conditions and sintered material properties on the linear accuracy and the creation of internal defects. Predictions are made of the distortion in manufacture of simple features such as cylinders and steps, as a first step to using the tool to develop strategies for improved processing.

Selective laser sintering (SLS) is one of a group of rapid prototyping technologies developed over the last ten years to build objects directly from a three-dimensional computer aided design (CAD) model without the need for tooling. The CAD model is sliced into a stack of layers and each layer in turn is converted to a physical layer, bonded to the preceding layer. In the stereolithography (SLA) process, a photosensitive polymer resin is converted to solid, layer on layer, using an ultraviolet laser beam scanning over the area of the slice. In the laminated object manufacturing (LOM) process, cut-to-shape laminates are bonded together. In fused deposition manufacturing (FDM), tracks of thermoplastic are laid down from a scanning extrusion head to build up layers. In three-dimensional printing (3DP), layers are created from powders, on to which a traversing ink jet head prints a bonding agent. SLS is a thermal process, creating layers by melting powders, or partially melting powder mixtures, by a scanning infrared laser beam [**1**–**3**].

Objects made by these layer manufacturing processes are used for the following:

(a) visualization, marketing and verification of design intent (all the processes are suitable for this);
(b) functional testing when their physical or mechanical properties are suitable (for example polyamide SLS parts for testing the performance of polyamide parts eventually to be injection moulded);
(c) making sacrificial patterns for investment casting (SLA, SLS, LOM);
(d) making investment casting shells or patterns for sand casting directly (SLS, LOM, 3DP); and
(e) recently for making injection mould and pressure die casting tooling directly from metal powders (SLS) [**2**, **3**].

However, none of the processes are as accurate as machining. It is difficult to achieve linear accuracies of ± 0.1 mm [**1**, **4**]. There are three general sources of inaccuracy:

1. There can be errors of approximation in converting the CAD model to slice data.
2. There can be machine control errors.
3. There can be processing errors in converting feed material to its finished state.

SLS can have two types of processing error, stemming from its thermal nature:

1. Parts cooling down to room temperature can shrink and distort.
2. There are offset errors both normal to and in the planes of the layers.

An analogy may be made with the action of an end-milling cutter used to machine a cavity: the path of the cutter centre must be offset, by its radius and half its thickness, from the surface to be machined. A laser is a thermal tool. The effective radius of the tool and also its length will increase as the peak temperature that it creates increases. This paper is concerned with modelling the SLS process to understand better both what controls powder densification and offset accuracy and what is necessary for accurate modelling. Predictions from modelling are compared with experimental observations. In this paper, SLS of only the thermally most simple, amorphous powders is considered. Then there is no latent heat absorption/evolution on the liquefaction/solidification of the powder. Simulation results and experimental observations are obtained for a polycarbonate polymer that is commercially available for processing by SLS.

The general situation of the SLS to be modelled is shown schematically in Fig. 1a. The powder bed sits on a piston. It is preheated to a temperature just below the glass transition temperature of the powder by heaters of power q_r. An infrared laser beam directed by a scanning mirror delivers extra power P to the bed surface to create the part layer. Every time a new layer is to be added, the piston is moved downwards by one layer thickness and a new layer of powder is spread over the surface: building always occurs in the plane $z = 0$. Figure 1b shows the surface layer in plan. The laser beam of diameter d scans at speed U in the $\pm x$ direction, over the current width w of the layer, and rasters with a spacing s in the $+y$ direction (s is shown greater than d in Fig. 1b, for ease of drawing, but in practice there is overlap between rasters). The processed front moves at speed $V = s(U/w)$ in the $+y$ direction. In the present work some simplification is introduced into the general

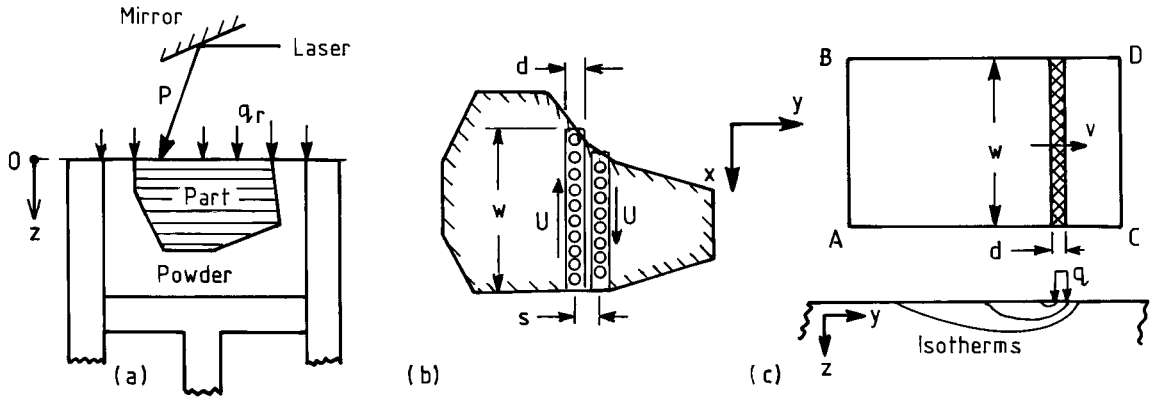

Fig. 1 Schematic views of the selective laser sintering process

three-dimensional temperature modelling of the process. The actual scanning laser spot is replaced with a rectangular source of width w and breadth d, moving at speed V. The heat per unit area, q, of this equivalent source is related to P by the requirement that the equivalent and real sources deliver the same heat to the part:

$$q = \frac{P}{Us}\frac{V}{d} \tag{1a}$$

The simplification is valid when the speed U is large enough for the raster cycle time w/U to be much less than the time d^2/κ for heat to diffuse d [**5**]:

$$U >> \frac{\kappa w}{d^2} \tag{1b}$$

A second simplification is made for convenience. In all the modelling to be reported, only parts of constant width w are considered. Figure 1c shows one layer of such a part, with, schematically, the subsurface temperature distribution to be calculated.

Previous work by other authors has mainly been limited to one-dimensional temperature modelling [**6**]. Away from part edges, the major temperature gradient is in the z direction. One-dimensional modelling, with a heat source active for a time (beam diameter/beam speed) can give a good prediction of temperature/time variations. However, it is not able to address edge effects. That is the new contribution of the present paper. Temperature modelling has been performed in three different ways using classical (analytical), finite difference and finite element methods. It is concluded that, for accurate modelling, the variation in the thermal properties of a material with density as it converts from powder to solid must be taken into account, so finite difference or finite element methods are necessary. The analytical method can give reasonable agreement with experiments if an appropriate choice of average thermal property is made. However, what is appropriate depends on whether the prediction of density or size accuracy is the purpose of the analysis. Some of this work has been published before in conference proceedings [**5**, **7**–**9**]. With the passage of time, some assumptions made initially have been proved to be unfounded; some errors have been detected. Where information in this paper contradicts that in earlier papers, the present work overrides earlier studies. The development of the modelling is described in Section 2, and a range of experiments both to obtain physical property data for modelling and to test the modelling procedure is presented in Section 3. Results of the experiments are given and compared with predictions in Section 4. A broader discussion of the results, including an analysis of the sensitivity of predictions to changes in sintering conditions, is given in Section 5.

2 THEORY

An account of the physical phenomena to be modelled and their governing equations is followed by sections on how these equations have been solved.

2.1 Physical model

Figure 2a shows the sintering of a first layer of powder by a laser beam. Material shown hatched has sintered

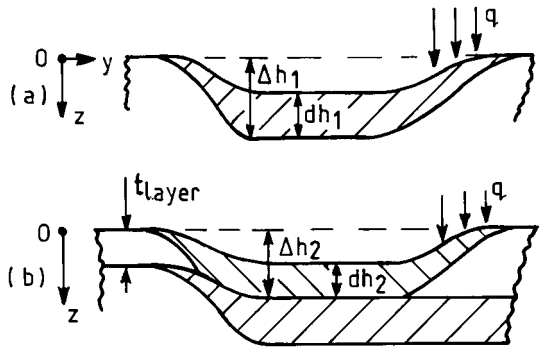

Fig. 2 Sintering of (a) a first and (b) a second layer of powder

to a depth Δh_1 depending on the temperature field created by the laser and the dependence of sintering on temperature and time. As a result it has shrunk to a thickness $\mathrm{d}h_1$. The powder bed surface has become depressed by $\Delta h_1 - \mathrm{d}h_1$. Figure 2b shows the sintering of a second layer, with its edge vertically above the first layer. Away from the first layer it is t_{layer} thick (a typical value is 0.125 mm) but over the first layer it is thicker than this because of the shrinkage of the first layer: $\Delta h_2 = t_{\text{layer}} + \Delta h_1 - \mathrm{d}h_1$. As a result of sintering, it shrinks to a thickness $\mathrm{d}h_2$. If the process is repeated for i layers, eventually a steady state is reached, with Δh_i becoming independent of i, and $\mathrm{d}h_i = t_{\text{layer}}$. Assuming that shrinkage results only in material movement in the z direction, the average density in any layer i is found from mass conservation:

$$\rho_{\text{average}} \mathrm{d}h_i = \rho_{\text{powder}} \Delta h_i \tag{2a}$$

Mass conservation also determines $\mathrm{d}h_i$ from the variation in density with z within the ith layer:

$$\mathrm{d}h_i = \int_0^{\Delta h_i} \frac{\rho_{\text{powder}}}{\rho(z)} \, \mathrm{d}z \tag{2b}$$

The dependence of Δh_i on i is summarized as follows:

$$\text{if } i = 1, \qquad \Delta h_i = \text{function of process} \tag{2c}$$

$$\text{if } i > 1, \qquad \Delta h_i = t_{\text{layer}} + \Delta h_{i-1} - \mathrm{d}h_{i-1} \tag{2d}$$

Therefore, for every layer except the first one, equation (2d) gives Δh_i and then equation (2b) gives $\mathrm{d}h_i$ if the variation in density with z is found; finally (2a) gives the average density of the layer. These equations also apply near the edges of a part, where Δh_i and $\mathrm{d}h_i$ vary with y. Thus variations in layer density round part y edges can be estimated. Shrinkage in the first layer is found directly from equation (2b) after determining Δh_1 by inspection.

The variation in density with z has been calculated using a viscous sintering law [(equation (3)] following Nelson *et al.* [**6**]. These authors have given values of A and E/R for polycarbonate as $A = 8.84 \times 10^{16}\ \mathrm{s}^{-1}$ and $E/R = 21\,000\ \mathrm{K}^{-1}$. Density $\rho_{\max}$ is an adjustable constant. It is the density achievable in an infinitely long sintering time: its maximum value is that of the fully dense material, but a lower value would be appropriate if at some value $\rho_{\max}$ the sintering mechanism changed to give a much larger value of E/R:

$$\frac{\mathrm{d}\rho}{\mathrm{d}t} = (\rho_{\max} - \rho) A \mathrm{e}^{-E/(RT)} \tag{3}$$

The temperature/time histories of elements in the powder bed, needed for integration of equation (3), have been found by solving the heat conduction equation for a moving heat source and with the conductivity k allowed to vary with position and temperature (sintered material has a greater conductivity than the initial powder and its presence greatly influences the heat flow). The boundary conditions have been: no heat loss from the free surface boundary; all other boundaries held at ambient temperature. The equation with axes fixed in the heat source and the powder bed moving at speed V in the $+y$ direction is as follows:

$$\rho C \frac{\partial T}{\partial t} = k \nabla^2 T + \frac{\partial k}{\partial T} \nabla T \nabla T + \nabla k \nabla T - \rho C V \frac{\partial T}{\partial y} \tag{4}$$

(when axes are fixed in the powder bed, the convection term is omitted and the heat source becomes a moving heat flux boundary condition). The specific heat C for polycarbonate, from reference [**6**], has been assumed to vary with temperature:

$$C\ (\mathrm{J/kg}) = 935 + 2.28T(\mathrm{K}) \tag{5a}$$

The conductivity k of solid polycarbonate has also been taken from reference [**6**]:

$$k_{\text{solid}}(\mathrm{W/m\ K}) = 0.0251 + 0.0005T(\mathrm{K}) \tag{5b}$$

The variation in k with density (or porosity ε), the source of its variation with position, has been assumed to be given by

$$\frac{k}{k_{\text{solid}}} = 1 - a\varepsilon - b\varepsilon^2 \quad \text{where } \varepsilon = \frac{(\rho_{\text{solid}} - \rho)}{\rho_{\text{solid}}} \tag{5c}$$

and coefficients a and b are determined experimentally (Sections 3 and 4). The relation, derived from equation (5c), between the variation in k with position and the variation in density with position is given by

$$\frac{\partial k}{\partial x(y \text{ or } z)} = \frac{k_{\text{solid}}}{\rho_{\text{solid}}}(a + 2b\varepsilon) \frac{\partial \rho}{\partial x(y \text{ or } z)} \tag{5d}$$

The variation in conductivity with temperature, derived from equations (5c) and (5b), is given by

$$\frac{\partial k}{\partial T} = 0.0005(1 - a\varepsilon - b\varepsilon^2) \tag{5e}$$

2.2 Solution methods

Three strategies for solving equations (2) to (4) in order to investigate density variations over a part have been studied. In the first, classical moving heat source theory has been used to solve an approximate form of equation (4), neglecting variations in k but making various choices for it, then equations (3) and (2) have been applied to estimate densification and shrinkage, as described in Section 2.2.1. In Section 2.2.2, equations (3) and (4) have been solved simultaneously using an adaptive mesh finite difference code with error control in both space and time; then equation (2) has been applied to estimate shrinkage. Finally (Section 2.2.3) a finite element procedure has been implemented in which temperature, density and shrinkage changes in the powder bed are followed sequentially as time increases in fixed steps.

2.2.1 *Classical moving heat source method*

The temperature in a semi-infinite medium of constant thermal properties, moving at speed V past a source of width d and length w (Fig. 1c), supplying heat q uniformly for time $t > 0$, has been given by Jaeger [**10**]. In a coordinate system (x, y, z) the origin of which is fixed in the centre of the heat source

$$T = \frac{\alpha q}{V}\frac{\kappa/k}{2\sqrt{(2\pi)}}\int_0^{V^2t/2\kappa}\frac{e^{-Z^2/2u}}{\sqrt{u}} \times\left[\operatorname{erf}\frac{X+B}{\sqrt{(2u)}}-\operatorname{erf}\frac{X-B}{\sqrt{(2u)}}\right] \times\left[\operatorname{erf}\frac{Y+L+u}{\sqrt{(2u)}}-\operatorname{erf}\frac{Y-L+u}{\sqrt{(2u)}}\right]du \quad (6)$$

where

$$X=\frac{Vx}{2\kappa},\qquad Y=\frac{Vy}{2\kappa},\qquad Z=\frac{Vz}{2\kappa},\qquad L=\frac{Vd}{4\kappa}$$

and

$$B=\frac{Vw}{4\kappa}$$

Provided appropriate values of κ and k are chosen, equation (6) may be used in five ways:

1. Setting $x = 0$ and $t = \infty$, the steady state variation in temperature with y at constant depths z beneath the surface can be calculated. At each depth z the final density can be calculated by numerical integration of equation (3) along y, noting that material moves a distance dy in time $dt = dy/V$. The values thus found for $\rho(z)$ can be substituted in equation (2b) to find the value of Δh_i that yields $h_i = t_{\text{layer}}$. These values can then be substituted in equation (2a) to give an estimate of the part density due to sintering far from surface regions.
2. The same procedure can be followed for values of x in the neighbourhood of $\pm w/2$ to study variations in density round part edges normal to x (BD or AC in Fig. 1c).
3. Temperature/time histories and hence density variations in the neighbourhood of starting edges (AB in Fig. 1c) can be followed by calculating temperature variations with position and time as t increases from zero.
4. In the neighbourhood of stopping edges (CD in Fig. 1c), temperature/time histories can be found by imagining a heat source of strength $-q$ suddenly added to the steady state solution of strength $+q$.
5. Finally, the calculation of density variation with z in case (1) may be used directly to study the thickness of first-sintered layers (Fig. 2a).

All these have been done, calculating temperatures over x, y and z and carrying out numerical integrations of equation (3) along y at intervals $dx = dy = dz = 0.025$ mm: this compares with values in the experimental work of $t_{\text{layer}} = 0.125$ mm and $d = 0.4$ mm.

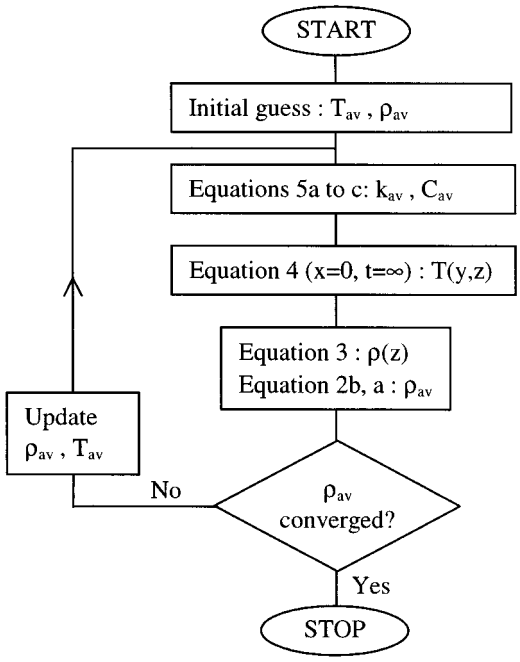

Fig. 3 Flow chart of the iterative analytical computation

Two groups of choices of κ and k have been made:

1. Values for powder have been used to obtain an upper limit to the temperature and sintering estimates. Equations (5a) to (5c) have been used for C and k, with $\rho = \rho_{\text{powder}}$ and T set (with insight from later work) at 350 °C.
2. For a range of values of q [equation (1a)] and V, and given values of w and d, values of κ and k have been found that yield temperature/time histories in the powder bed that, with procedure 1 above, lead to average densities in the part consistent with the chosen κ and k [through equations (5a) to (5c)].

The flow chart in Fig. 3 explains the procedure. An initial guess of average temperature T_{av} and density ρ_{av} is made for substitution in equations (5a) to (5c) for average values of k and C and hence, with ρ_{av}, of κ. The average temperature is defined, somewhat arbitrarily, as the mean of the ambient bed temperature and the peak temperature caused by the laser heating. Equation (4) is solved with $x = 0$ and $t = \infty$ to obtain the steady state temperature distribution in the powder bed along the centre-line of a part such as that in Fig. 1c. Equations (3) and (2) are then applied to estimate average density in a steady state layer ($dh = t_{\text{layer}}$). If this density differs by more than 1 per cent from the input density, the calculation is repeated with updated values of average density and temperature.

2.2.2 *Adaptive mesh simultaneous finite difference method*

An overview of the scheme for the finite difference based calculation is given in Fig. 4. Initial conditions of density are defined in the powder bed and the limits of movement of the laser over the bed for the current layer are specified. When the first layer of a part is being created, a uniform density powder bed is set up. After that, the bed contains density variations as prescribed by previously sintered layers. At the start of a calculation, the bed is assumed to have its ambient temperature.

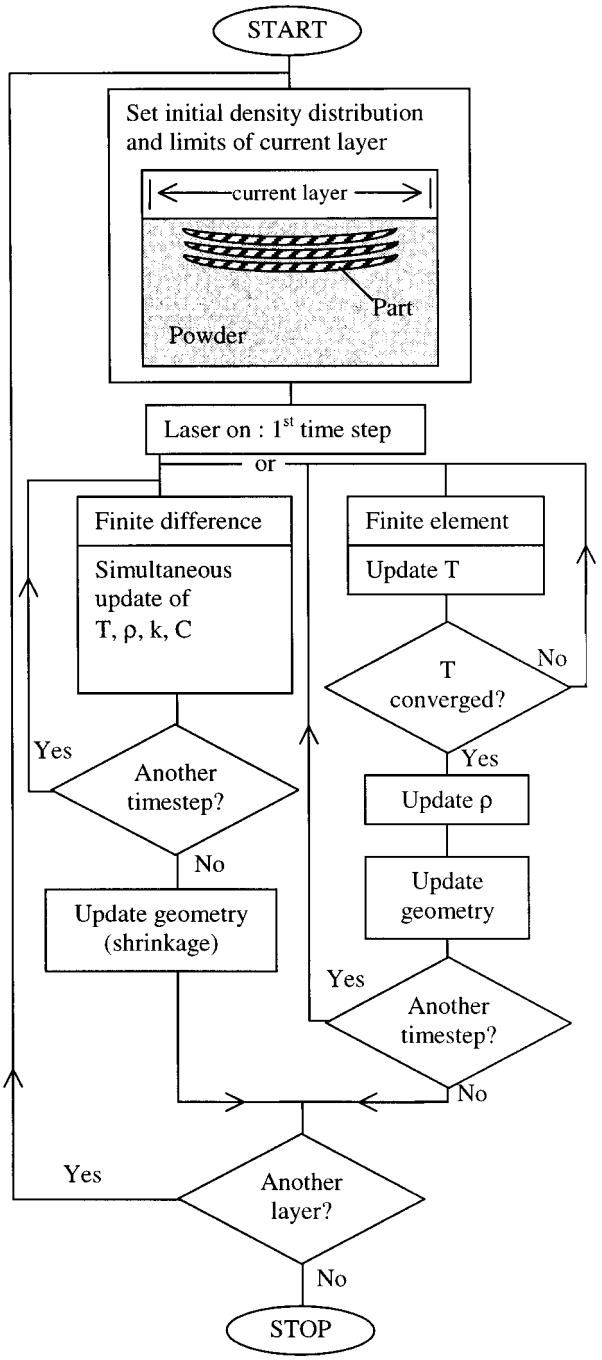

Fig. 4 Flow charts of the finite difference and finite element computations

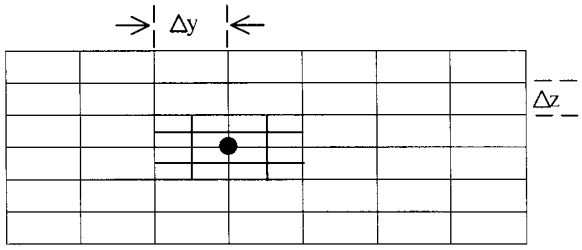

Fig. 5 Part of the initial finite difference mesh, with one level of refinement around node ●

Equations (3) and (4), linked by equations (5), are then solved simultaneously over the time interval from beginning to end of the laser movement (in this case, axes have been assumed fixed in the powder bed, with the laser moving over it, so the convection term of equation (4) has been omitted). In this calculation, k and C changes due to densification and temperature variation are fully considered, but the geometry change due to shrinkage is ignored. Shrinkage, according to equation (2b), is calculated after the laser has completed the current layer. Therefore ρ in the heat capacity term ρC of equation (4) has been held constant at its initial value throughout the temperature calculation.

The simultaneous calculation of the variation in temperature and density with position and time has been implemented only in two dimensions (in the yz plane), using software code VLUGR2 (vectorizable local uniform grid refinement for partial differential equations in two dimensions) developed and supplied by Blom *et al.* [**11**]. The actual implementation takes porosity and not density as the dependent variable. Dependence of temperature and porosity on position is calculated over a spatial mesh which is automatically refined according to the sizes of the spatial second derivatives of the variables; dependence on time is calculated at time intervals that depend on the time rate of change in the variables.

Mesh refinement. At the start of each time step the current values of temperature and porosity are discretized at the nodes of an initially uniform rectangular grid of spacing Δy and Δz covering the problem space (Fig. 5). Standard second-order finite difference approximations to the temperature and porosity spatial second derivatives are created, central within and one-sided on the boundaries of the domain. At each node the spatial variation monitoring quantity, $m_{s,i}$, is evaluated:

$$m_{s,i} = \frac{\alpha_{s,i}}{U_{\max,i} T_s} \left[(\Delta y)^2 \left| \frac{\partial^2 U_i}{\partial y^2} \right| + (\Delta z)^2 \left| \frac{\partial^2 U_i}{\partial z^2} \right| \right] \tag{7}$$

where $i = 1$ or 2. When $i = 1$, U_i refers to temperature and $U_{\max,i}$ is the approximate maximum expected

temperature. When $i = 2$, U_i and $U_{\max,i}$ refer to porosity. Quantities $\alpha_{s,i}$ and T_s are weighting and tolerance factors respectively. If the value of $m_{s,i}$ exceeds 1.0 at any node, the mesh is automatically refined around that node, as shown for one level of refinement, at one node, in Fig. 5. The quantities Δy and Δz, α_i and T_s, $U_{\max,i}$ and the maximum number of levels of refinement are set by the user.

Time refinement. Partial differential equations (3) and (4) are solved by spatial discretization using finite difference methods and then by numerical integration with respect to time, as an initial value problem, over time steps Δt. Time integration is by a second-order backward difference method, the system of non-linear equations at each time step being solved by a Newton-GMRES iteration [**11**]. After each time step the time monitoring quantity, $m_{t,i}$, is estimated at each node of the refined mesh:

$$m_{t,i} = \frac{\alpha_{t,i}}{U_{\max,i} T_t} \Delta t \left| \frac{\partial U_i}{\partial T} \right| \tag{8}$$

where the quantities have analogous definitions to those in equation (7). If any value of $m_{t,i}$ exceeds 1.0, the integration is rejected, the time step is halved and the integration is repeated. Factors $\alpha_{t,i}$ and T_t are set by the user. Further details of the use of VLUGR2 are given in reference [**11**].

2.2.3 *Sequential thermal finite element and densification method*

The strategy of the finite element scheme differs in its layer sintering part from that of the finite difference scheme (Fig. 4). Temperature, density and geometry changes are calculated sequentially within each time step. The temperature is calculated iteratively with an implicit update of thermal properties, as will be explained. Furthermore, the meshes over which the calculations are performed are not adaptively varied. Rather, they vary in size according to a predetermined scheme.

The y–z cross-section of a powder bed (Fig. 6a) is created as an array of rectangular elements initially each of length $d/6$ in the y direction and $t_{layer}/6$ in the z direction and assigned a density equal to that of the powder. A part definition is created in the bed. Layer by layer, the definition is converted to a part by the operation on it of the thermal finite element, densification and shrinkage calculations. Figure 6a shows the situation of a part for which two layers (hatched) have already been built and a third layer is being created.

Figure 6b shows details of the thermal mesh. In the neighbourhood of the heat source q, which is given a Gaussian width distribution, the thermal mesh maps exactly on to the powder bed mesh. It coarsens with distance from the heat source in multiples of the powder bed mesh size until, in the corner diagonally opposite the heat source, one thermal mesh element contains three rows and 256 columns of powder bed elements. Linear interpolations are used to map between the powder bed and thermal meshes. In all, the thermal mesh was chosen to be up to $12 \times t_{layer}$ deep (depending on laser power) and approximately $90d$ long. In one time step, a displacement of $d/6$ takes place.

Each four-node brick of the thermal mesh is regarded as a pair of three-node triangles, such as A and B with nodes ijk and lmn in Fig. 6b. In this most simple type of element, variations in k and C can be accommodated by assigning an average value [depending on the average element temperature and its density, equations (5a) to (5c)] to each element, allowing discontinuity in k and C between elements (C_0 continuity in T). The k varying terms in equation (4) can then be omitted from the element thermal stiffness equation. The time marching scheme

$$\left([\bar{K}]\theta + \frac{1}{\Delta t}[\bar{C}] \right) \{T\}_{t+\Delta t} = \left(\frac{1}{\Delta t}[\bar{C}] - (1-\theta)[\bar{K}] \right) \{T\}_t - \{F\} \tag{9a}$$

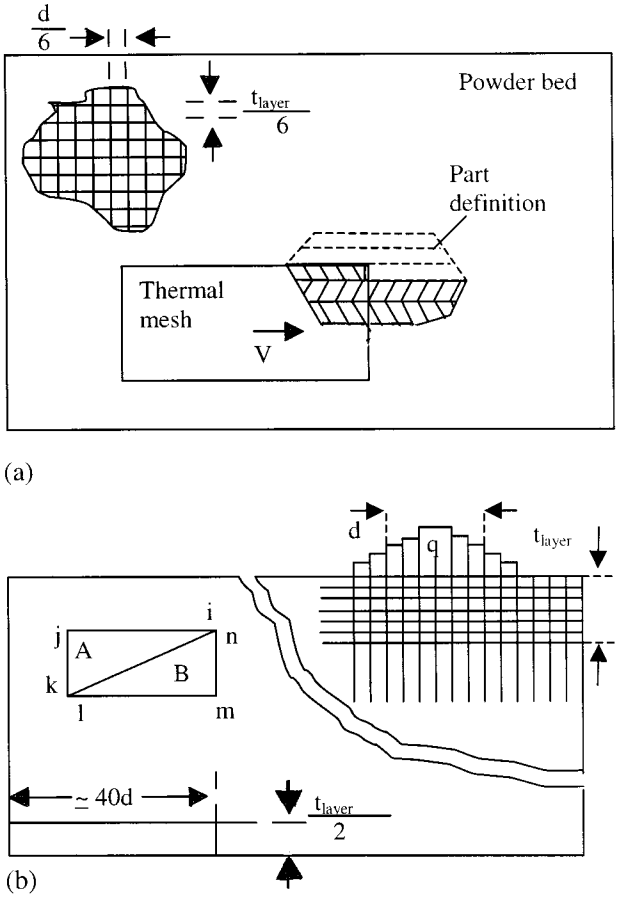

Fig. 6 Overviews of (a) the powder bed and (b) the thermal finite element meshes

Table 1 User-defined variables held constant in the adaptive mesh method

Quantity	$i=1$	$i=2$
α_s	1.0	0.7
U_{max}	600 °C	0.6
α_t	1.0	0.7

where

$$[\bar{K}] = (1-\theta)[K]_t + \theta[K]_{t+\Delta t}$$
$$\text{and} \tag{9b}$$
$$[\bar{C}] = (1-\theta)[C]_t + \theta[C]_{t+\Delta t}$$

for calculating T at time $t+\Delta t$ from that at time t has been implemented, following reference [**12**], with $\theta = 0.878$ and $[K]$, $[C]$ and $[F]$ adapted from an existing moving heat source finite element temperature calculation [**13**]. As indicated previously, this calculation is performed iteratively. The values of k and C at time $t+\Delta t$, needed to evaluate $[K]_{t+\Delta t}$ and $[C]_{t+\Delta t}$, are obtained from the temperatures of the previous iteration, from equations (5a) to (5c), and also from updated densities. Densities are updated in the thermal mesh by applying equation (3) in the form

$$\rho_{t+\Delta t}\left(1+\theta_s A \mathrm{e}^{-E/(RT_{t+\Delta t})}\Delta t\right) = \rho_t\left[1-(1-\theta_s)A\mathrm{e}^{-E/(RT_t)}\Delta t\right] + \rho_{max}\left[(1-\theta_s)A\mathrm{e}^{-E/(RT_t)} + \theta_s A \mathrm{e}^{-E/(RT_{t+\Delta t})}\right]\Delta t \tag{10}$$

again with $\theta_s = 0.878$. Equations (9) are solved by the lower–upper decomposition (LUD) method. After convergence of temperature in the thermal mesh, updated temperatures are returned to the powder bed mesh, with interpolation as necessary. Equation (10) and equations (2) are then applied on the powder bed mesh to update its density and geometry. At the next time step, these updated densities and geometries are fed back to the thermal mesh.

2.3 Computational testing

Before the solution methods of the last section were compared with experimental results, their stability and sensitivities to internal variables and differences between them were studied. In the adaptive meshing calculation (Section 2.2.2) the number of levels of mesh refinement was set at 3 in order to avoid excessive CPU time and use of storage. Other user-defined computational variables held constant after initial testing are given in Table 1. The influence of varying the initial grid size from 0.12 to 0.6 mm (for Δy) and from 0.03 to 0.15 mm (for Δz) and of varying T_s and T_t from 0.01 to 1 is reported in Section 4.2. The range of Δy gave a range from 0.015 to 0.075 mm at the third level of refinement and was chosen to cover expected levels of part resolution in the physical process. The smaller values of Δz, refining down to the range 0.004–0.02 mm, were chosen to reflect the small layer thicknesses (0.125 mm) in the physical process.

In the finite element calculation, the effect of varying the θ and θ_s parameters, from 0.875 down to a value of 0.7, was found to have no significant effect on the results. The effect of varying how the thermal mesh size increased with distance from the heat source is reported in Section 4.2, as is a comparison of the predictions of all three computational methods.

3 EXPERIMENTATION

3.1 Sintering experiments

Simple parts have been manufactured from commercially supplied polycarbonate powder in a commercial laser sintering machine. At an early stage, rectangular blocks $25 \times 90 \times 6.4$ mm thick (z) were made, mainly to study the dependence of part density, linear accuracy and mechanical properties on operating conditions; the sides of the blocks were aligned with the x and y directions (Fig. 1). These will be referred to as series 1 blocks. Later (series 2), after hardware and software control upgrades of the machine, further blocks were made, but their dimensions were $25 \times 25 \times 2$ mm thick. The hardware upgrade was a more precise scanning mirror (Fig. 1a) control system. The software upgrade was to improve beam diameter compensation in offsetting the laser scan path from the part edges. Also later, a range of hollow cylinder and T-piece shapes were made, to study form errors.

In all cases, manufacture took place in an inert atmosphere, of nitrogen, with the ambient temperature of the powder bed held nominally at 154 °C (a recommended temperature, a few degrees below the glass transition temperature of the polycarbonate). The part layer thickness was always 0.125 mm and the quoted Gaussian beam diameter of the CO_2 continuous wave laser was 0.4 mm.

The parts were made at various laser powers, scan speeds and scan spacings, from 6 to 14 W, 520 to 1200 mm/s and 0.1 to 0.4 mm respectively, to give energy densities $P/(Us)$ delivered by the laser of 0.035–0.125 J/mm^2. (Previous work [**5**, **8**, **9**] and the structure of equation (6), with equation (1a), suggests that, for a given beam diameter, sintering depends on the laser scanning variables mainly through $P/(Us)$). The first layer of a part was supported in position in the powder bed by a standard method, by building it on a base. A base is a two-layer thick platform, lightly sintered [$P =$ 13 W, $U = 1200$ mm/s, $s = 0.63$ mm, giving $P/(Us) =$ 0.017 J/mm^2] marginally to increase the cohesion of the

powder immediately below the main part. Subsidiary experiments on the influence of a base are introduced in Section 4.3.

Before each set of tests, calibration tests were carried out in the standard operating conditions with $P/(Us) = 0.063$ J/mm^2 to minimize errors in part size (in the standard conditions) arising from shrinkage in cooling to room temperature and from wrong settings of beam offset compensation. A testpiece with a range of x and y linear dimensions of 10–100 mm was manufactured. Measured errors in x and y were plotted against the expected value, leading to a measured slope (rate of change in error with expected value) and zero intercept (value of error at zero expected value). Shrinkage and offset compensations were applied to reduce the slopes and zero intercepts to zero [with $P/(Us) = 0.063$ J/mm^2].

3.2 Subsidiary experiments

3.2.1 *Physical property measurements*

The theory of Section 2 requires inputs of powder bed density, maximum sintered density [in equation (3)] and thermal conductivity parameters a and b [equation (5c)]. These quantities have been measured. The theory also needs the sintering parameters A and E/R [equation (3)] and the solid polycarbonate thermal properties k and C [equations (5a) and (5b)]: these values have been assumed, as already stated. It also needs a value of absorption coefficient α [as in equation (6), but also used in the finite difference and element calculations]: a value of 0.95 has been taken from reference [**6**].

Powder bed density was measured by manufacturing, at different places in the bed, fifteen hollow cylindrical cups, bottom-down, of 22 mm internal diameter and 15 mm internal height. Afterwards, they were carefully removed, with unsintered powder intact in them. Removing the powder from each cup, weighing it and dividing by the internal volume of the cup enabled density to be estimated.

Maximum sintered density was determined by weighing and measuring the volume of heavily sintered parts. (It was observed that a plateau density, less than full density, occurred at high sintering energies, as considered further in Sections 4.1 and 4.4.)

The dependence of the thermal conductivity of polycarbonate on its sintered density was measured by a comparator method in a simple rig built for that purpose. In outline: a range of polycarbonate discs of approximately 70 mm diameter and 2–7 mm thickness were made with densities ranging from approximately 500 kg/m^3 (powder), through 530–910 kg/m^3 (sintered), to 1100 kg/m^3 (melted in a mould in an oven). These were each placed in contact with a comparator disc (machined from nylon). The pairs of discs were then sandwiched between an aluminium heater plate above and an aluminium heat sink plate below and surrounded circumferentially by thermally insulating glass wool. An electrical heater in the upper disc was adjusted to give temperatures in the polycarbonate in the range 50–100 °C. Thermocouples were placed in close-fitting grooves at the interfaces between the polycarbonate, nylon and aluminium surfaces and the thermal conductivity of the polycarbonate relative to the nylon was estimated from the ratio of the measured thermal gradients across them.

3.2.2 *Sintered part measurements*

The x, y and z dimensions of the blocks were measured with a flat-ended micrometer and linear errors were established by subtracting from these the expected dimensions. The blocks were weighed and their densities calculated by dividing by the volume estimated from the product of the x, y and z measured lengths.

The microstructure and edge details of representative samples of all parts were observed in an optical microscope, after mounting the parts in a thermosetting resin, sectioning and polishing them. The dependence on part density of Young's modulus, yield stress and failure stress was determined by four-point bend tests on the $25 \times 90 \times 6.4$ mm blocks. These observations were compared with predictions from the methods described in Section 2.

4 RESULTS

4.1 Densities and thermal conductivities

The fifteen powder bed density measurements gave a range of 465–505 kg/m^3 with a mean value of 485 kg/m^3. The measured density of the most heavily sintered parts was only 1000 kg/m^3 (compared with an expected theoretical density of 1200 kg/m^3). Microscopic observation showed the reason for this to be that such parts contained pores, typically of 20–80 μm diameter (an example will be shown as part of Fig. 11), perhaps caused by the degassing of water or other vapours during sintering.

Figure 7 shows in relative terms how the thermal conductivity of the polycarbonate varied with its density. The scatter in values comes in part from an observed small dependence of estimated conductivity on sample thickness, an effect of thermal contact resistance between the samples in the test rig so low, compared with the random scatter, that it has not been felt worthwhile to correct for it. A regression analysis gives values of -0.20 and $+1.73$ to coefficients a and b in equation (5c). The values determined in this section, with others assumed as described in Section 3.2.1, are used in the following calculations.

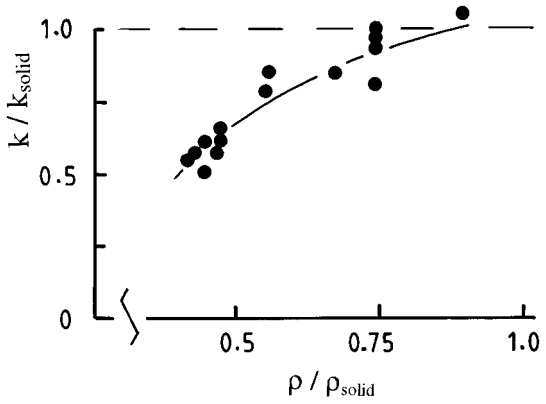

Fig. 7 Density dependence of polycarbonate conductivity at temperatures of 50–100 °C

4.2 Computational comparisons

Initial calculations with the adaptive mesh finite difference method showed that the choice of Δy, in the range 0.12–0.6 mm, had little effect on solution stability or accuracy. However, from the point of view of a short solution time, there was a weak optimum around $\Delta y = 0.2$ mm, at which there were fewest rejected integration steps on the basis of excessive size of the time monitor m_t [equation (8)]. It is perhaps significant that 0.2 mm is half the laser beam diameter. Likewise, there was an optimum choice, on the basis of time, of $\Delta z = 0.04$ mm; but, in addition, larger values of Δz did not allow sufficient resolution in z for accurate calculation of densification and layer thickness from equation (2): $\Delta z = 0.04$ mm is about half the sintered layer thickness. The choice of space and time refinement tolerances T_s and T_t was critical to successful calculation. If either were 0.5 or above, there would be possibilities of solution instability. As they were reduced together to 0.05, the number of rejected integrations decreased; further reductions below 0.05 simply resulted in smaller time steps and a longer solution time. In subsequent work, the following values are used: $\Delta y = 0.2$ mm, $\Delta z = 0.04$ mm and $T_s = T_t = 0.05$.

These values of Δy and Δz may be compared with the smallest unit sizes in the structured thermal finite element mesh of $d/6 \approx 0.07$ mm and $t_{layer}/6 \approx 0.02$ mm, reducing to ≈ 0.01 mm after sintering. It can be seen that the finest thermal finite element mesh size was around the second level of refinement of the finite difference mesh. In testing how the choice of thermal mesh affected predicted sintering, it was observed that, as the temperature front associated with starting the laser scan convected through the mesh at velocity V, the region of fine y spacing of $d/6$ had to be extended to keep up with it, until the temperature had decreased below the sintering temperature range. Otherwise, temperature instabilities led to false estimates of y oversize.

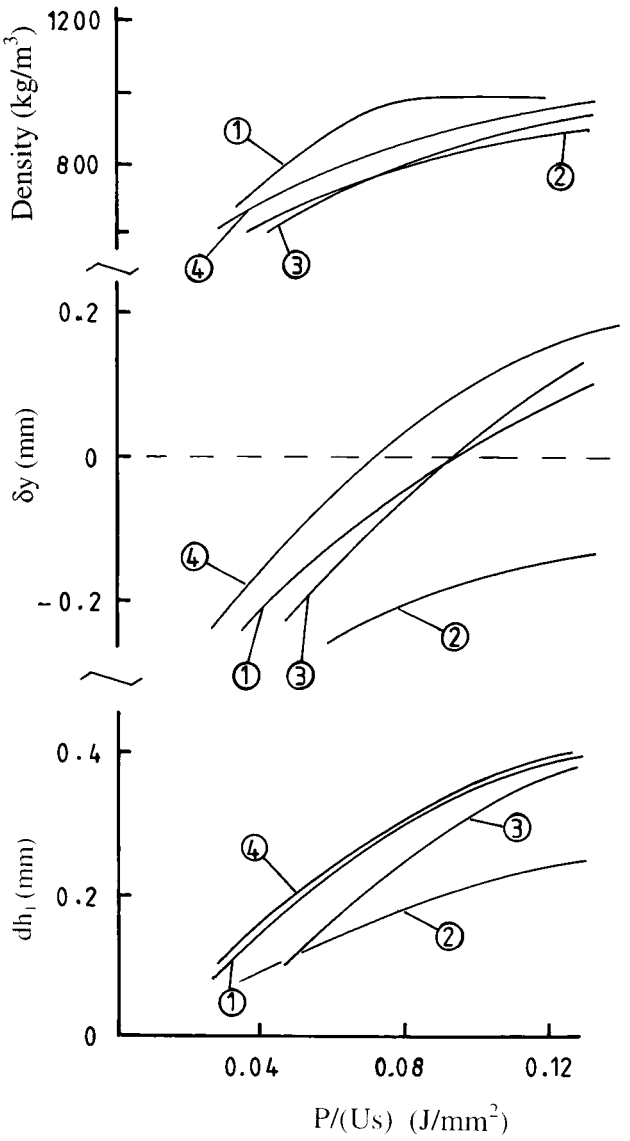

Fig. 8 Dependence of part density, y oversize and first-layer thickness on $P/(Us)$, determined analytically with (1) constant and (2) iterated powder thermal properties and by (3) the finite difference and (4) the finite element method

Density, y oversize and first-layer thickness predictions from all three computational methods are compared in Fig. 8. In constructing the y oversize and first-layer thickness predictions, it has been assumed that the edge of a part is defined by a sintered density of 500 kg/m^3. Other choices give systematically different predictions, as considered briefly in Section 5, but do not affect the following observations. The finite element method closely follows the finite difference method but gives slightly larger predictions of density, y oversize and first-layer thickness. This is consistent with its slightly coarser mesh (compared with the third level of refinement of the finite difference mesh) but is hardly significant compared with other sources of

uncertainty, as will be seen later. The analytical method was in agreement with the finite difference and finite element methods over density prediction if the thermal properties used were chosen by iteration to be self-consistent with the densification; there was also agreement over y oversize and first-layer thickness prediction if thermal properties of the unsintered powder were used.

4.3 Density and oversize comparisons with experiment

Figure 9 compares the finite difference and finite element density predictions with measurements from the series 1 and series 2 tests. The predicted values are in accord with the series 1 tests but are systematically greater than the series 2 results. The reason lies in the basis of comparison. The predicted values are densities within the bulk of a part; the measured values are the average of the bulk and a less dense lower surface region. All the measured parts had a z thickness greater than expected (to be discussed in reference to Fig. 10); if their densities are recalculated using expected thicknesses, the series 1 and 2 results come together within the theoretically expected band.

Figure 10 compares predicted and measured part oversizes. The top panel shows that measured oversize in the y direction was the same for series 1 and 2 tests and varied with $P/(Us)$ as expected from the finite difference (3) and finite element (4) theories. In constructing the theoretical lines, the edge of a part was again assumed to occur at a density of 500 kg/m^3: with this choice the finite element predictions better match the measured values. The scatter of experimental measurements is $\approx \pm 0.05$ mm, the limit of linear accuracy of the sintering process in the present machine.

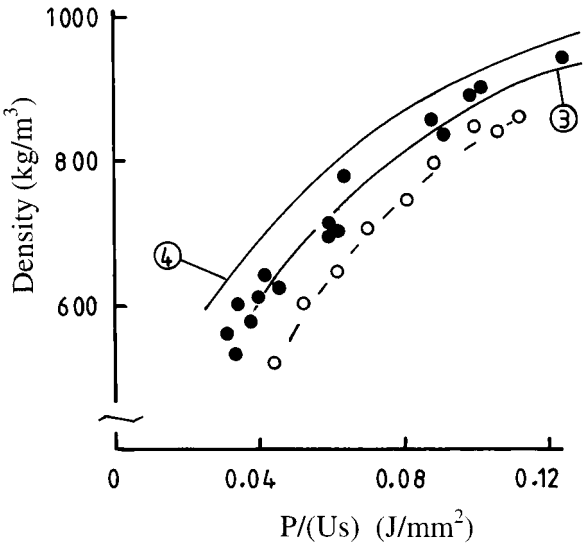

Fig. 9 Observed part densities from series 1 (●) and series 2 (○) tests, compared with the computed values from curves 3 and 4 in Fig. 8

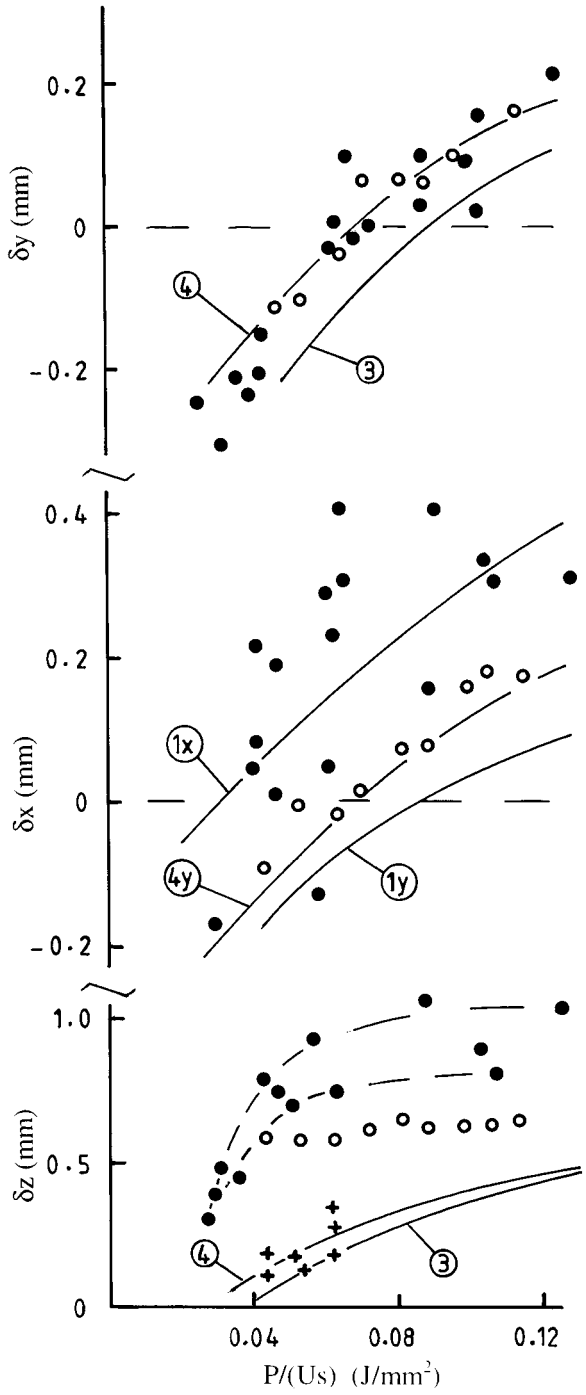

Fig. 10 Observed y, x and z oversize from series 1 (●) and series 2 (○) tests [and also for δz from other tests (+)], compared with predicted values as explained in the text

The middle panel presents x oversize results. As only the analytical calculation is three-dimensional, its prediction of oversize (line 1x based on unsintered powder thermal properties) is included in the figure. The analytical prediction for y oversize is added as line 1y and the y oversize prediction from the finite element calculation is copied from the top panel as line 4y. For a given

laser beam offset, x oversize is predicted to be greater than y oversize at any given $P/(Us)$. The series 1 measurements show this and are also seen to be much more widely scattered ($\approx \pm 0.1$ mm) than the y oversize measurements. However, the series 2 measurements cluster around the 4y line and are less scattered too, a result of the hardware and software upgrades referred to in Section 3.1.

The bottom panel records z oversize observations. The finite difference and finite element predictions (lines 3 and 4) are the extent to which the 500 kg/m^3 first-layer density contour projects into the powder bed below the geometrical first layer of 0.125 mm thickness. The series 1 and 2 measurements are both greater than predicted, and the series 1 measurements are greater than the series 2 measurements, except at the lowest energy densities. However, in a subsidiary set of tests in which the supporting base beneath a block was replaced with a flange around the edge of the block to enable base-free measurements to be made, z oversize measurements more closely followed theory ($+$). It is speculated that the series 2 tests resulted in a larger than theoretical z oversize because of the influence of bases. The only known difference between the series 1 and 2 blocks is that their thicknesses were different. The series 1 blocks would have been heated by sintering for about three times as long as the series 2 blocks (6.4 mm thickness compared with 2 mm): perhaps their z oversize, larger than the series 2 blocks, occurred owing to a secondary sintering due to overheating of powder trapped under the blocks.

4.4 Mechanical property and simulated microstructure studies

The left-hand column in Fig. 11 records the various mechanical properties measured in four-point bend testing as a function of measured specimen density. Simulated density contours (schematic microstructures) at three energy densities are reproduced in the bottom right-hand column, with two examples of actual microstructures above.

Mechanical failure (bottom left) occurred by crumbling at the lowest densities (marked C), by layer delamination (L) at intermediate densities and by tensile fracture (B) at the highest densities. The simulated microstructures (bottom right) are in accord with these observations. At an energy density of 0.031 J/mm^2 the sintered layers are shown hardly connected, at 0.063 J/mm^2 the layers are just connected and at 0.089 J/mm^2 the layers are shown almost fully merged.

The simulations (all of which refer to a nominal part length of 5.4 mm) show two further features. Firstly, there is an increase in thickness of the first sintered layer and of y oversize with increasing energy density. The direction of laser travel over the powder was from left to right: it is particularly interesting that the y oversize occurs predominantly at the laser start position. This assymetry of oversize could have implications in developing beam offsetting rules or could influence scanning strategies to be alternately left to right and right to left. The vertical faces also differ in profile between laser start and laser end positions, the more so the higher the energy density: the profiles at the start are more bluff and at the end are more prow-shaped. Secondly, even at the highest energy density shown, the second layer is not sintered to the first as well as subsequent layers are to each other (marked A in the figure). The first sintered layer is associated with a larger surface sinking ($\Delta h_1 - \mathrm{d}h_1$) than subsequent layers, so the second spread powder layer is thicker than subsequent ones. The first layer has sufficient thermal mass to quench the full sintering of the second layer, whereas subsequently the more thinly spread powder layers are more completely through-sintered.

The actual microstructures (top right) confirm the clearly layered and totally joined layers at the intermediate and high energy densities. The micrograph for 0.063 J/mm^2 shows the difference between the actual particulate state of the microstructure and the continuum simplification of the simulation. The 0.131 J/mm^2 microstructure shows the porosity that has previously been considered in Section 4.1.

Figure 12 shows further simulated microstructures of a hollow cylinder nominally of 10 mm outer and 4 mm inner diameter. It contains 77 layers. The complete cylinder is shown for an energy density of 0.031 J/mm^2 and magnified views of parts of the cylinder are shown for higher energy densities. In all cases the laser scanned from left to right. The bore of the cylinder is not circular. At its top dead centre the layer that closes the bore sinters as a first sintered layer with z oversize. At the top of the figure, increasing flattening of the top of the bore with increasing energy density is shown. Feature A is the same undersintering effect marked as A in Fig. 11. The same z oversize effect causes the bottom left quadrant of the cylinder to bulge (marked B in the bottom left of the figure), also with an A defect. Two further effects, C and D, are shown in the middle left panel of the figure. To the right of the bottom of the bore, the laser-start sintered profile at C has the same prow shape as the laser-stop profile to the left. This is in contrast to the bluff start profile in Fig. 11 and is due to the quenching effect of the previously sintered layers extending to the left of the laser-start position. Around the region marked D, consecutive pairs of layers appear preferentially blended. This is a discretization effect, the result of approximating the circular bore to a stepped profile in determining the laser-start positions.

A further example of the effects of first sintered layer z oversize is shown in Fig. 13. This is a T-piece, both the stem and arm of which are five layers thick. If the

first layer of the arm is followed along its length, it can be seen that it is at a lower z position where it overhangs powder than where it is above the stem. This is as expected from the modelling represented in Fig. 2. As a result, at the joins of the arm to the stem, as seen more clearly in the magnified views as features B, layers merge with one another to a greater degree than elsewhere.

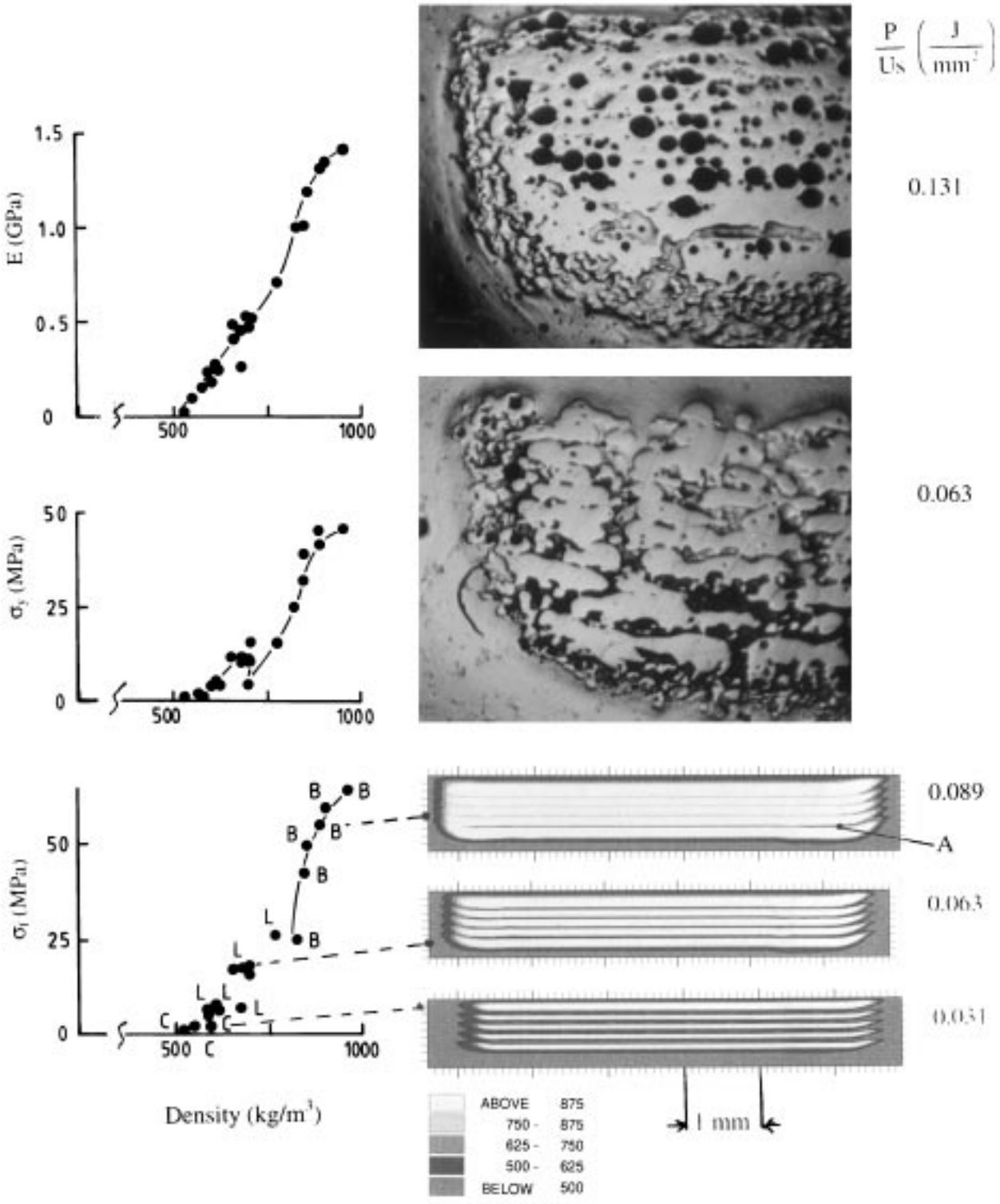

Fig. 11 Observed part mechanical property dependence on density (left column) and simulated five-layer thick and observed ten-layer thick microstructures (right column)

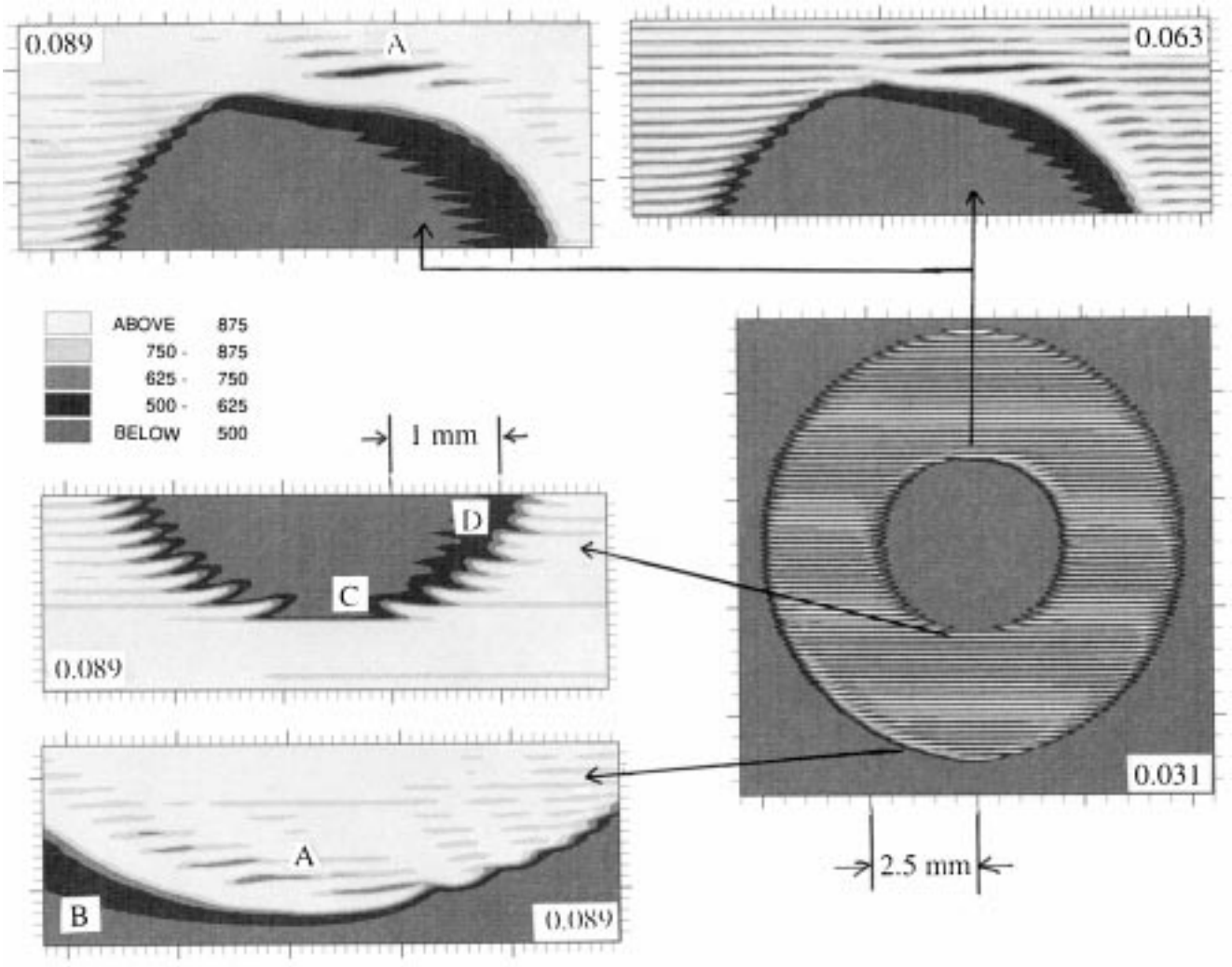

Fig. 12 Simulated hollow cylinder manufacture at different energy densities (J/mm^2) as labelled

5 DISCUSSION

A first step has successfully been taken in the process modelling of selective laser sintering of an amorphous polymer, as a result of which part microstructure and edge features, as well as densification and linear accuracies, can now be simulated. Three alternative thermal models have been tested within the simulation. The most simple has been an analytical model. It has given good estimates of densification in an iterative implementation designed to select thermal conductivity and heat capacity values consistent with the densification. It has given good estimates of x, y and z oversize when thermal properties of the unsintered powder have been used. It is quick to use and is the only version that is three-dimensional at the present time, but it is unable to predict the fine detail of features such as those revealed in Figs 12 and 13, nor is it likely to be extendible to the treatment of crystalline materials. The finite difference and finite element methods need no user choice to be made of thermal properties. The adaptive meshing feature of the finite difference method used makes it more robust at the cost of requiring greater computing power. The accuracy of the finite element formulation relies on user judgement with respect to its mesh size but requires less computing power (77 layer thick hollow cylinders have been simulated with the finite element approach for this reason). A choice cannot be made between the finite difference and finite element methods on the basis of better agreement with experiment, since (as will be shown below) differences between their predictions are smaller than can be created by variations within the uncertainty of available data.

Table 2 shows the sensitivity of densification and linear accuracy to changed processing and other parameters, as predicted by the finite element version of the simulation. The activation energy ratio E/R has the largest influence on predictions. Changes of ± 10 per cent in this ratio cause density and size variations greater than the differences between the finite difference and finite element predictions. Next in importance is the influence of specific heat C. This comes through its

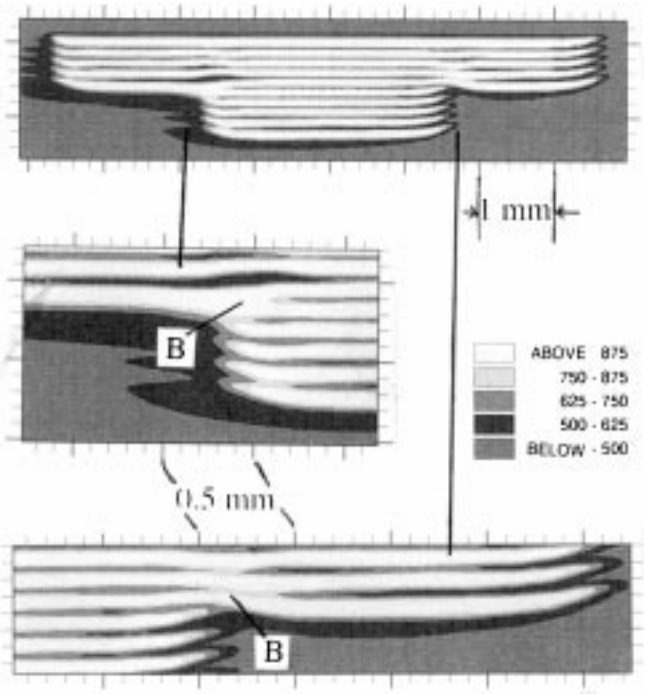

Fig. 13 Simulated T-piece manufacture at an energy density of 0.063 J/mm^2

influence on the heat capacity of the sintered part. The main cause of non-linearity in the thermal analysis comes from the difference in heat capacity, as a result of densification, between a sintered part and the powder from which it is created. A ± 10 per cent variation in C causes density and size changes of the order of the scatter in physical observations.

Powder bed density ρ_{powder} is the next most important variable. In Table 2 the influence of a 5 per cent change is shown (whereas other variables are tested with a 10 per cent change). This is because 5 per cent variations were measured to occur. Furthermore, only -5 per cent is tested; $+5$ per cent brings ρ_{powder} to more than 500 kg/m^3, the level at which the program judges a part edge to be sintered. With hindsight, this judgement would better be framed not as an absolute value but as relative to ρ_{powder}. The layer thickness has a similar level of importance. (There is no effect on z oversize as, during sintering of the first layer, the powder depth is not restricted by the layer thickness.) The possibility of increasing ρ_{max} by reducing whatever causes the residual porosity in heavily sintered parts (Fig. 11) has a small effect on densification but hardly any effect on oversize.

Table 2 Finite element sensitivity analysis concerning the standard conditions of Section 4.3 and $P/(Us) = 0.063$ J/mm^2

Quantity and % change	Consequent change in		
	Density (kg/m^3)	δy (mm)	δz (mm)
E/R, $\pm 10\%$	-90, $+120$	-0.18, $+0.55$	-0.13, $+0.24$
C, $\pm 10\%$	-21, $+25$	-0.04, $+0.03$	-0.03, $+0.03$
ρ_{powder}, -5%	-10	-0.03	-0.04
t_{layer}, $\pm 10\%$	-21, $+25$	-0.02, $+0.00$	± 0.00
ρ_{max}, $+10\%$	$+31$	$+0.01$	$+0.00$
A, $\pm 10\%$	$+3$, -2	± 0.01	± 0.00
k_{solid}, $\pm 10\%$	± 0.00	-0.02, $+0.01$	± 0.00
$a = 0.5$, $b = 0$	-13	-0.04	-0.02
Edge density, $+10\%$	0	-0.08	-0.1

The Arrhenius coefficient A has little effect on the process, as does the thermal conductivity of the solid material, k_{solid}. The latter is at first surprising in view of the influence of C. It indicates that in the transient heating conditions of the process it is the influence of heat capacity on heating rate rather than heat loss that controls temperature rise. The model of how thermal conductivity varies with part density is more important. In earlier publications [**7–9**], coefficients a and b in equation (5c) were assumed (without any evidence) to be 0.5 and 0 respectively. Table 2 shows how these values lead to slightly changed predictions.

The final row of Table 2 considers the influence on oversize prediction of changing the definition of a part edge from the 500 kg/m^3 density contour to 550 kg/m^3. The oversize is reduced by about the difference between the predictions of the finite element and finite difference based models. There is no independent evidence of which is the more realistic edge density criterion. The two numerical models cannot be differentiated by comparison with experiment. Either can be used: the finite element implementation has been preferred for the sensitivity analysis because of its lesser computing power requirements.

Table 2 contains no comparisons of the effects of varying laser power, scan speed or scan spacing. These can be deduced from Fig. 8. A 10 per cent change in any one causes a 10 per cent change in $P/(Us)$. From the figure, such a change causes a 30 kg/m^3 change in density, a 0.03 mm change in y oversize and a 0.02 mm change in z oversize. These are of the same order as many of the Table 2 effects: only the sensitivity to change in activation energy is clearly larger. It might be concluded, after noting that the random scatter in physical measurements is around ± 30 kg/m^3 and ± 0.05 mm, that ± 5–10 per cent is currently the range within which many of the process variables are controlled.

Apart from the material processing factors that have just been discussed, the experimental work has highlighted other factors that influence accuracy. The difference between the series 1 and 2 x oversize measurements indicates the importance of machine control factors, both hardware and software, in realizing the process potential. The z oversize observations are

more varied than the x and y oversize ones. The series 2 results direct attention to the building of strategies in which bases are not needed or are localized at a few sacrificial pinning points. It is not certain why the series 1 observations differed from those of series 2: possibly there are other processing factors in play such as secondary sintering caused by overheating of the powder bed beneath downward facing flat surfaces, where cooling by convection may be impeded.

Although the present work has been successful in its modelling of amorphous polymers, it is only a first step. There are still many further steps to be added before a complete tool kit exists to support selective laser sintering process improvement. These must include modelling part distortion from residual stresses and their relaxations. This will need the present local heat conduction thermal model for predicting sintering temperature/time histories to be coupled to a spatially larger thermal model of the whole build volume, to include convective heat transfer, in order to determine temperature/time transients around the glass transition temperature. Another direction will be to extend the modelling, by the inclusion of latent heat effects, to the sintering of crystalline materials such as the practically important polyamides. Finally, the thermal properties of polymers that allow two-dimensional modelling to be adequate [through satisfaction of equation (1b)] differ from those of metals: a similar approach to that used in the present paper for simulating the selective laser sintering of metals will certainly need three-dimensional modelling.

6 CONCLUSIONS

Simulations of the selective laser sintering of polycarbonate have been created using analytical, adaptive mesh finite difference and fixed mesh finite element methods. Predicted part densification, linear accuracy and microstructural features have been found to be in good agreement with experiments. Key to the success has been accounting for the non-linear thermal properties of the polymer that arise from its increasing density during sintering.

Sensitivity studies, using the predictions of the finite element simulation, have shown that the factors that influence process accuracy, in decreasing order of importance, are the sintering activation energy of the polymer, the specific heat of the polymer, the powder bed density, the powder layer thickness and the maximum density achievable by sintering (which may be less than the fully solid density because of porosity caused by outgassing of the polymer under high laser powers). The experimental studies have also shown the importance of machine hardware and software control features and base build effects in influencing part accuracy, in addition to the inherent material processability factors that are the main subject of this paper.

ACKNOWLEDGEMENTS

Parts of this work were supported by the European project EUREKA EU776 'The Integration of CAD, CAE and Fast Free Form Fabrication'. One of the authors (G.R.R.) is grateful to the University of Leeds Keyworth Institute for Manufacturing and Information Systems Engineering for a scholarship. The authors also wish to thank Dr K. W. Dalgarno and Mr A. Marsden for many helpful discussions.

REFERENCES

1 **Kruth, J.-P.** Material incress manufacturing by rapid prototyping techniques. *Ann. CIRP*, 1991, **40**(2), 603–614.
2 **Jacobs, P. F.** *Stereolithography and Other RP&M Technologies*, 1996 (ASME Press, New York).
3 **Beaman, J. J., Barlow, J. W., Bourell, D. L., Crawford, R. H., Marcus, H. L.** and **McAlea, K. P.** *Solid Free Form Fabrication*, 1997 (Kluwer Academic Publishers, Dordrecht).
4 **Childs, T. H. C.** and **Juster, N. P.** Linear and geometric accuracies from layer manufacturing. *Ann. CIRP*, 1994, **43**(1), 163–166.
5 **Childs, T. H. C., Cardie, S.** and **Brown, J. M.** Selective laser sintering of polycarbonate at varying powers, scan speeds and scan spacings. In Proceedings of 5th Solid Freeform Fabrication Symposium (Eds H. L. Marcus *et al.*), Austin, Texas, 1994, pp. 356–363 (University of Texas at Austin, Austin).
6 **Nelson, J. C., Xue, S., Barlow, J. W., Beaman, J. J., Marcus, H. L.** and **Bourell, D. L.** Model of the selective laser sintering of bisphenol-A polycarbonate. *Ind. Engng Chem. Res.*, 1993, **32**, 2305–2317.
7 **Ryder, G. J., Berzins, M.** and **Childs, T. H. C.** Modelling simple feature creation in selective laser sintering. In Proceedings of 7th Solid Freeform Fabrication Symposium (Eds J. W. Barlow *et al.*), Austin, Texas, 1996, pp. 567–574 (University of Texas at Austin, Austin).
8 **Berzins, M., Childs, T. H. C.** and **Ryder, G. R.** The selective laser sintering of polycarbonate. *Ann. CIRP*, 1996, **45**(1), 187–190.
9 **Childs, T. H. C., Ryder, G. R.** and **Berzins, M.** Experimental and theoretical studies of selective laser sintering. In Proceedings of 8th International Conference on *Production Engineering* (Eds N. Ikawa, T. Kishinami and F. Kimura), Hokkaido, 1997, pp. 132–141 (Chapman and Hall, London).
10 **Jaeger, J. C.** Moving sources of heat and the temperature at sliding contacts. *J. R. Soc. New South Wales*, 1942, **76**, 203–224.

11 **Blom, J. G., Trompert, R. A.** and **Verwer, J. G.** Algorithm 758 VLUGR2: a vectorisable adaptive grid solver for PDEs in 2D. *ACM Trans., Math. Soft.*, 1996, **22**, 302–328.

12 **Tszeng, T. C., Im, Y. T.** and **Kobayashi, S.** Thermal analysis of solidification by the temperature recovery method. *Int. J. Mach. Tools Mfg*, 1989, **29**, 107–120.

13 **Childs, T. H. C., Maekawa, K.** and **Maulik, P.** Effects of coolant on temperature distribution in metal machining. *Mater. Sci. Technol.*, 1988, **4**, 1006–1019.